SWIMSAT: A Real-Aperture Radar to Measure Directional Spectra of Ocean Waves from Space—Main Characteristics and Performance Simulation

DANIÈLE HAUSER

CETP/CNRS, Velizy, France

ELBATOUL SOUSSI

CLS, Ramonville St. Agne, France

ERIC THOUVENOT

CNES, Toulouse, France

LAURENT REY

Alcatel Space Industries, Toulouse, France

(Manuscript received 27 July 1999, in final form 31 March 2000)

ABSTRACT

The project SWIMSAT aims to measure the directional spectra of waves from space using a real-aperture radar with a low-incidence, conical-scanning beam. This system's design is based on airborne versions developed in France and the United States. In this paper, the authors present the satellite measurement principle and instruments. For this study, the authors developed a simulation method to analyze the sensitivity of wave spectra, taking into account radar observation conditions (spatial resolution, signal-to-noise ratio, integration time, etc.) and inversion processing parameters (noise level and range displacements during temporal integration). The simulation method and results are presented in this paper. The study enabled validation and refinement of the satellite concept. The simulations show that in the chosen configuration, SWIMSAT is capable of measuring wave spectral properties in wind–sea conditions (at dominant wavelengths over approximately 70 m) and swell conditions (at significant wave heights over approximately 1.5–2 m, depending on wind). Unlike for synthetic aperture radar observations, the performance of SWIMSAT in terms of minimum detectable wavelength is independent on the wave propagation direction.

1. Introduction

Today, most operational meteorology centers use numerical models to provide ocean wave predictions. However, unlike atmospheric circulation models, wave prediction models do not incorporate a lot of observations to constrain their variables. Data assimilation in wave prediction models is most frequently based upon observations of the total energy (or significant wave height) of the wave spectrum, ignoring their spectral properties (Janssen et al. 1989; Lionello and Günther 1992; Breivik and Reistad 1994; Mastenbroek et al. 1994). In these studies, radar altimeter data of significant wave heights are commonly used. The main drawback of these methods, based on the assimilation of total energy alone, is that they need certain assumptions about the characteristics of the wave field, and in particular, the separation between swell and wind–sea. This might generate errors or reduce the impact of the assimilation. Recent studies (de la Heras et al. 1994; Voorrips et al. 1997; Breivik et al. 1998) have shown that the assimilation of spectral information improves the prediction, even though they concern small geographical zones (e.g., part of the North Sea or Norwegian Sea). They also show that to improve numerical wave predictions, spectral information is necessary to decrease errors due to either the model itself (parameterizations, numerical uncertainties) or the forcing surface wind field. For ocean basin predictions, only satellite data can provide observations compatible with the large-scale forecast.

Synthetic aperture radar (SAR) is currently the only technology for estimating directional ocean wave properties from a spaceborne sensor. But SAR has one major drawback: it is now well known that the wavelike patterns visible in SAR images of the ocean surface may be considerably different from the actual ocean wave field. As a result, extracting meaningful two-dimen-

Corresponding author address: Dr. Danièle Hauser, CETP, 10-12 Avenue de l'Europe, 78140 Velizy, France.
E-mail: hauser@cetp.ipsl.fr

sional wave spectral properties from a SAR scene is not straightforward. The SAR's ability to provide usable ocean wave spectra is limited by the motion of the ocean surface. Doppler misregistrations in azimuth (along-track) are induced by motions of the scatters, leading to a distortion of the imaged spectrum and a strong cutoff in the azimuth direction. This effect is proportional to the range-to-velocity ratio of the platform. For present and future missions (ERS, Radarsat, Envisat), this ratio is high (about 120 s), thus considerably limiting the usefulness of SAR products. In particular, inversion of SAR data into wave spectra is based upon a first guess, usually provided by wave models (Hasselmann and Hasselmann 1991; Krogstadt et al. 1994; Brüning et al. 1994; Engen and Johnsen 1994, 1995; Hasselmann et al. 1996). Using such SAR products for assimilation in the same models is therefore not completely independent of the model itself. Another drawback is that information provided by SAR is limited to long wavelengths. This limit depends on the relative direction of wave propagation with respect to satellite track. In the case of waves propagating in the along-track direction, only waves longer than 150–200 m are detectable. As a result, the usefulness of SAR measurements is open to debate, and such measurements are not yet widely used in the engineering or forecasting community.

For all these reasons, our group has been working since the beginning of the 1990s on the design, development, and use of radar systems conceived to measure directional wave spectra using the real-aperture technique in place of the SAR technique. In the 1990s, a new airborne radar system called RESSAC (Radar pour l'Etude du Spectre de Surface par Analyse Circulaire) has been used during several joint experiments (validation campaigns of the *ERS-1* satellite in 1991, SWADE in 1991, SEMAPHORE in 1993, and FETCH in 1998). The good results this system has obtained (Hauser et al. 1992a,b; Hauser and Caudal 1996; Eymard et al. 1996; Hauser et al. 1995) as well as those achieved by a NASA group with a similar system (ROWS; Jackson et al. 1985; Jackson and Walton 1985) led us to propose a radar based on the same measurement principle (Soussi 1997). The project SWIMSAT (Surface Waves Investigation and Monitoring from SATellite), formerly called VAGSAT, has been conceived as a dedicated mission on board a small satellite mission.

The measurement principle of SWlMSAT is based on existing airborne radar systems: RESSAC (Hauser et al. 1992a) and ROWS (Jackson et al. 1985; Jackson and Walton 1985). In section 2, we describe how directional wave spectra are measured and present the main features of the SWIMSAT system. To conduct a detailed study of SWIMSAT's performance and to factor in the perturbing effects of different noise sources, we developed a numerical simulation. Section 3 explains the successive steps in the simulation process, that is, simulation of the ocean surface, radar observations, factoring of perturbing effects (speckle noise, thermal noise, displacement of the radar footprint), and inversion of observations in terms of wave spectra. The results, detailed in section 4, were obtained for a version of the instrument that guarantees the required level of geophysical performance while reducing the number of technical constraints as far as possible. These results also demonstrate the need to apply corrections within the inversion algorithms to take speckle noise, thermal noise, and displacement of the radar footprint into account.

2. SWIMSAT measurement principle and instrument features

The proposed system is a dual-beam radar (capable of nadir viewing and off-nadir viewing at an angle of 10°) operating in the K_u frequency band (13.565 GHz) and flying on a polar-orbiting satellite at an altitude of 450–600 km (Fig. 1). The nadir beam is operated to measure significant wave height and wind speed in the same way as spaceborne altimeters. SWIMSAT's innovative feature is its ability to operate in off-nadir viewing mode by tilting the radar beam 10° to measure wave spectral characteristics. This is the feature we will be focusing on in this paper. The principle is based on measuring modulations of the radar backscatter coefficient inside the swath covered by the 10° tilted beam. To acquire measurements in all directions of wave propagation, the 10° beam is rotated to perform a conical scan around the vertical axis (Fig. 1). This beam scanning is obtained by using an offset parabolic antenna, rotating only the feed horn, while keeping the parabole fixed. The satellite's altitude was determined by trading off the swath covered by a single conical scan of the beam, the power budget, and the satellite's design lifetime. We chose a mean altitude of 500 km, which corresponds, assuming a 10° incidence angle, to a swath of 88 km in radius, in order to be compatible with the resolution offered by wave prediction models (of the order of 1° lat × 1° long). This altitude also ensures that the power budget is compatible with measurement constraints (see section 2d) and a satellite lifetime of 3 yr or more.

a. Measurement principle

The measurement principle has been well documented in the literature (Jackson 1981; Jackson et al. 1985; Jackson and Walton 1985; Jackson and Lyzenga 1990; Hauser et al. 1992a). Here, we will focus our attention on the main features of this principle only. The reader is referred to the above papers for further details. The observation geometry is illustrated in Fig. 2.

At low incidence, the backscattering mechanism is dominated by quasispecular reflection from facets oriented perpendicular to the radar look direction. Facets with wavelengths larger than three to five times the electromagnetic wavelength contribute to this process. The normalized radar cross section σ_0 is related to the probability density function of the short waves forced

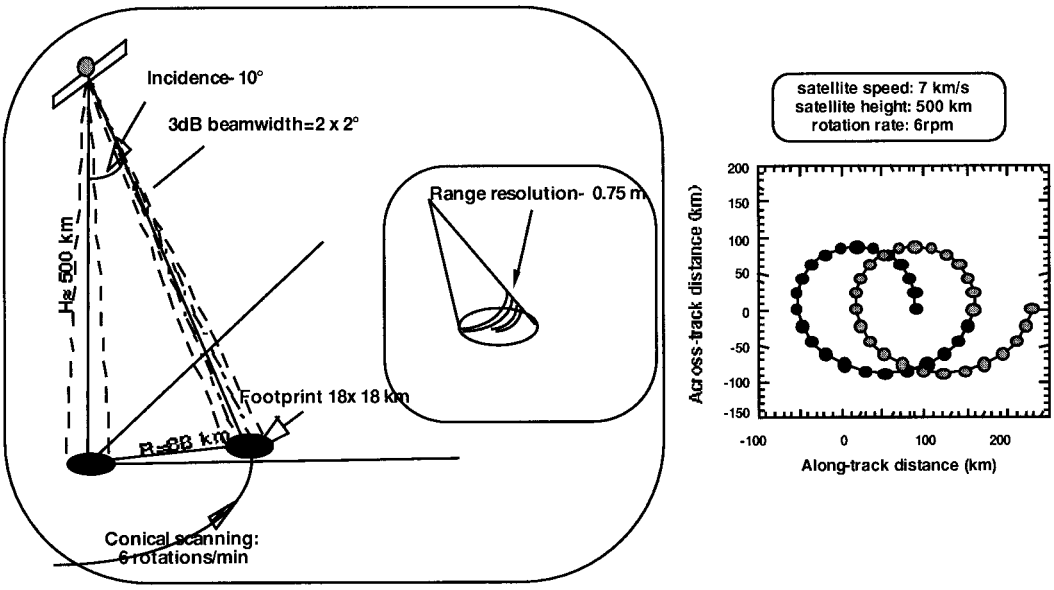

FIG. 1. Geometry of SWIMSAT. (a) Geometry of the twin-beam system. (b) View from top of the swath of the 10° incidence beam.

by the wind stress. This normalized radar cross section is modulated by the local slope of the surface due to the long waves. This is the so-called tilt modulation. The tilt modulation can be considered dominant and linear under the following conditions:

1) long-wave slope is small (less than 10%), which is a reasonable assumption for standard ocean waves;
2) hydrodynamic modulation is negligible; this process has been described extensively (Alpers et al. 1981) as a hydrodynamic effect that modulates the energy density of the capillary–Bragg waves along the long-wave profile; near 10° incidence angle, the backscatter intensity is almost independent upon roughness because the reflection conditions are intermediate between specular (where the backscatter intensity decreases with roughness) and Bragg (where the backscatter intensity increases with roughness); therefore, we can assume that for SWIMSAT, this hydrodynamic process has a negligible effect on the radar signal;
3) the footprint in the azimuth direction (L_y) is large with respect to the correlation length of the surface in the same direction; this assumption is valid when L_y is larger than the longer waves to be analyzed.

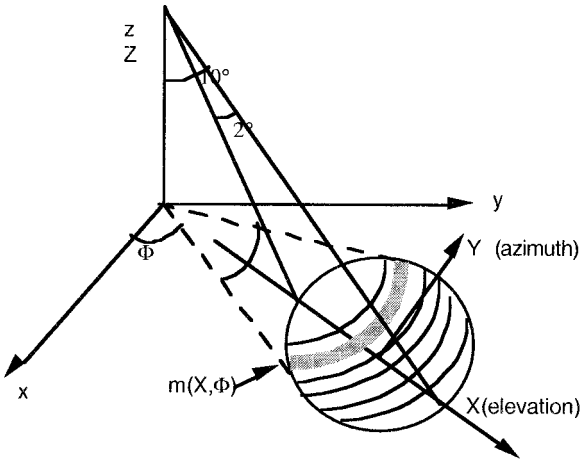

FIG. 2. Geometry for any given look direction ϕ. The elevation corresponds to the look direction axis OX. The azimuth is normal to this axis. The modulation $m(X, \phi)$ is defined for each look direction ϕ and as a function of the X coordinate of the OX axis.

b. Relationship between modulation spectrum and wave spectrum, with no noise

In quasispecular conditions, the radar cross section σ_0 is (Valenzuela 1978)

$$\sigma_0 = \frac{\rho\pi}{\cos^4\theta} p(tg\theta, 0), \tag{1}$$

where ρ is the Fresnel coefficient, θ is the incidence angle, and $p(tg\theta, 0)$ is the probability density of the presence of slopes perpendicular to the look direction in the plane of sight.

The relative variation in the backscatter coefficient σ ($\sigma = \sigma_0 S$) is expressed by

$$\frac{\delta\sigma}{\sigma} = \frac{\delta\sigma_0}{\sigma_0} + \frac{\delta S}{S}, \tag{2}$$

where S is the elementary surface corresponding to an individual radar range cell. Following Jackson (1981), Jackson and Walton (1985), and Jackson et al. (1985), each term on the right-hand side of Eq. (2) can be ex-

pressed in terms of the wave slopes in the look direction, $\xi_x(x, y)$. We thus obtain

$$\delta\sigma/\sigma(x, y) = \alpha\xi_x(x, y), \tag{3}$$

where α is given by

$$\alpha(\theta) = \cot\theta - 4tg\theta - \frac{1}{\cos^2\theta}\frac{\partial \ln p(tg\theta, 0)}{\partial tg\theta}. \tag{4}$$

From Eq. (3), we define the modulation of the backscattered signal in each horizontal radar cell and in a given look direction ϕ (see geometry in Fig. 2). This modulation is a quantity integrated over the resolution cell defined by the horizontal resolution dX and by the 3-dB aperture in azimuth (projected on the surface):

$$m(X, \phi) = \frac{\int G^2(\varphi)\frac{\delta\sigma}{\sigma}\,d\varphi}{\int G^2(\varphi)\,d\varphi} = \frac{\int G^2(\varphi)\alpha(\theta)\xi_X\,d\varphi}{\int G^2(\varphi)\,d\varphi}. \tag{5}$$

The Fourier transform of the autocorrelation function of $m(X, \phi)$ is the density spectrum of the modulation due to the tilt effect (see appendix). Assuming that the antenna gain pattern can be approximated by a Gaussian function and that the azimuth width of the radar footprint L_y is much larger than the correlation length in the azimuth direction, it can be shown that the transfer function between the modulation spectrum $P_m(k, \phi)$ and the wave-slope spectrum, $k^2F(k, \phi)$, is linear:

$$P_m(k, \phi) = \frac{\sqrt{2\pi}}{L_y}\alpha^2(\theta)k^2F(k, \phi), \tag{6}$$

where $F(k, \phi)$ is the wave-height spectrum in the look direction ϕ, and k is the wavenumber.

The scaling factor α is related to the slope probability density function (Eq. 4). However, since this function is wind-dependent and not measured directly, an estimate of α must be known to retrieve the slope spectrum of the waves from Eq. (6). Several methods can be used to achieve this. The first, developed and used for processing of airborne RESSAC data (Hauser et al. 1992a), consists of calculating α using the derivative of σ_0 with respect to the angle θ. This method requires an estimate of the mean profile of σ_0 over a wide range of incidence angles. Hence, it requires the use of a large beam aperture in the elevation direction and the calculation of the antenna gain for each point sampled horizontally, taking into account the attitude of the platform. For a spaceborne system, the power budget limits the beam width so that the range of incidence angles does not permit estimation of α. Therefore, for SWIMSAT, we propose to estimate α by normalizing the P_m values using an independent measurement of the significant wave height H_s, where H_s is related to the wave spectrum by

$$H_s = 4\sqrt{\iint F(k, \phi)\,dk\,k\,d\phi}. \tag{7a}$$

The nadir beam of SWIMSAT will measure H_s in the same way as for spaceborne altimeters (as on ERS or TOPEX/Poseidon). The value α is then given by

$$\alpha^2(\theta) = \frac{L_y}{\sqrt{2\pi}}\left(\frac{4}{H_s}\right)^2 \iint \frac{P_m(k, \phi)}{k^2}k\,dk\,d\phi. \tag{7b}$$

If there are no perturbing noise sources, the wave-height spectrum $F(k, \phi)$ in the look direction ϕ can be inverted from the modulation spectrum $P_m(k, \phi)$ using Eq. (6). To retrieve the full spectral information over all directions, a set of directions ϕ are sampled using a conical scan of the radar beam. Wavelength and direction resolutions depend on geometry, as shown by Jackson et al. (1985) and Jackson and Walton (1985). For a satellite configuration (high altitude), the resolution in direction depends to the first order on beam aperture in azimuth and on incidence angle only. For the configuration chosen for SWIMSAT, this leads to a resolution in direction better than 5°. We will see in section 4 that in order to decrease the statistical variability, we propose to degrade this intrinsic resolution to a 15° resolution (using averaging processes), still compatible with wave prediction models' performances and with the need for various applications. Concerning the wavelength resolution, it is inversely proportional, for each given wavenumber, to the length of the horizontal segment used to estimate the modulation spectrum analysis in the direction of look. For SWIMSAT, due to the large footprint dimension (18 km in length), this gives a theoretical resolution of the order of 1 m.

c. Noise contributions

A system such as SWIMSAT must be dimensioned to allow for perturbations likely to affect the wave spectrum we want to retrieve. Here, we shall describe the relation between the signal returned to the radar receiver and the modulation due to the wave-slope component, taking into account the radar characteristics and two noise sources (i.e., thermal noise and speckle). If there are no noise sources, the power, I, received at the receiver and backscattered from a radar cell of area dS, is expressed in terms of the transmitted signal power P_t, the electromagnetic wavelength λ, the target range R, and the two-way gain of the antenna:

$$I(R) = \frac{P_t\lambda^2}{(4\pi)^3R^4}\iint G_e^2(\theta)G_a^2(\varphi)\sigma_0\,dS, \tag{8}$$

where the two-way gain is defined as the product of the gains in azimuth $[G_a^2(\varphi)]$ and elevation $[G_e^2(\theta)]$. To express the modulation by the slopes of the longest waves, the radar cross section in Eq. (8) is written in terms of the modulation due to long-wave slopes, $\delta\sigma/\sigma$:

$$\sigma_0 = \tilde{\sigma}_0\left(1 + \frac{\delta\sigma}{\sigma}\right), \quad (9)$$

where the expression of $\delta\sigma/\sigma$ is given by Eq. (3) and $\tilde{\sigma}_0$ is the radar cross section we would observe if there were no long waves.

In Equation (8), we also assume that the integration element, dS, can be approximated by a rectangle of width dx and length dy, where $dx = c\tau/2\sin\theta$ and $dy = R\beta_\phi d\varphi$, c is the speed of light, τ the pulse duration, β_ϕ the antenna aperture in azimuth, and $d\varphi$ the 3-dB aperture in azimuth projected onto the sea surface.

By combining Eqs. (8) and (9) and the expressions for dx and dy, and assuming that R, $\tilde{\sigma}_0$ and $G_a^2(\theta)$ remain constant within $d\varphi$, we obtain

$$I(R) = \frac{P_t\lambda^2}{(4\pi)^3}\frac{1}{R^4}G_e^2(\theta)\frac{c\tau}{2\sin\theta}\beta_\phi R\tilde{\sigma}_0 \times \int G_a^2(\varphi)\left(1 + \frac{\delta\sigma}{\sigma}\right)d\varphi. \quad (10)$$

By substituting the function $C(R)$ for everything not in the integral, it becomes

$$I(R) = C(R)\int G_a^2(\varphi)\, d\varphi[1 + m(R)], \quad (11)$$

where $m(R)$ is the signal modulation due to the wave slopes:

$$m(R) = \frac{\int G_a^2(\varphi)\frac{\delta\sigma}{\sigma}\, d\varphi}{\int G_a^2(\varphi)\, d\varphi}. \quad (12)$$

In fact, the signal modulation $m(R)$ is affected by speckle, and $I(R)$ is affected by thermal noise. So, if we take these two noise sources into account, the backscattered power at range R is

$$I(R) = C(R)\int G_a^2(\varphi)\, d\varphi\{[1 + f[m(R)]\} + g(B_T), \quad (13)$$

where the function f describes the effect of speckle, and g is the effect of thermal noise.

d. Dimensioning of SWIMSAT

As a general rule, radars are predimensioned by applying a set of mission, geophysical, and technological constraints. Mission and system characteristics are a trade-off between these constraints. Below, we describe the main constraints and choices regarding SWIMSAT.

1) MISSION CONSTRAINTS

To increase the SWIMSAT project's chances of success, we decided to propose a system compatible with the so-called minisatellite platforms under development in various space agencies. In particular, the project was originally designed to be compatible with the 500 kg class PROTEUS platform of the French Space Agency (CNES). Of course, the present version of SWIMSAT is also compatible with larger platforms. Compatibility with minisatellite platforms requires a maximum electrical power of about 250 W and a maximum payload mass of about 100 kg. This led us to opt for a K_u-band radar with an antenna whose mass and dimensions satisfy these constraints. In order to optimize the ocean coverage, a polar orbit with an inclination close to 90° is chosen. To reduce onboard electrical power generation to a minimum, we propose that the satellite be fully powered by solar panels. The satellite will therefore be positioned in a sun-synchronous orbit with equator-crossing times of 0600 and 1800 UTC. This orbit is the preferred option but not absolutely imperative. The satellite altitude must be high enough to minimize problems caused by atmospheric friction and eclipse periods. An altitude of 450–600 km is a good trade-off given these constraints and the swath width (see below).

2) GEOPHYSICAL CONSTRAINTS

The measurement principle is based on a low-incidence look direction and a beam scanning through 360°. The satellite altitude must be such that the radar footprint is wide enough to analyze the longest waves and minimize statistical fluctuations but not so high that all azimuth directions within a single scan describe the same sea state. This last constraint led us to propose an altitude of about 500 km (600 km at the start of the mission, 450 km at the end if the orbit cannot be maintained). At a mean altitude of 500 km, the radius swept out by the near–nadir spectrum beam is 88 km. At this scale, one can consider that in most cases, the sea state is homogeneous. Therefore, we propose to use the nadir beam to estimate H_s by normalizing according to Eq. (7b). A mean altitude of 500 km also satisfies radar signal-to-noise ratio constraints (see below).

The thermal signal-to-noise ratio is a vital element of dimensioning calculations. This ratio is defined by $I(R)/B_T$, where $I(R)$ is given by Eq. (8), and the thermal noise B_T is given by

$$B_T = kTB_d, \quad (14)$$

where k is the Stefan–Boltzmann constant, T the system's equivalent temperature, and B_d is the transmission bandwidth. For dimensioning SWIMSAT, we initially chose an $I(R)/B_T$ above 3 dB at the edge of the 3-dB spot beam.

The received signal is affected by speckle noise, which is superimposed on the signal we want to analyze (modulations due to waves). We can show (see section 4 and appendix) that speckle imposes a detection threshold and introduces a bias into the estimate of the modulation spectrum due to waves. To minimize this speckle

TABLE 1. Mission and instrument characteristics.

Satellite	
Altitude	450–600 km
Orbit	Polar, sun synchronous
Antenna	
Type	Parabolic offset
Incidence (polarization)	0° (VV), 10° (HH)
Aperture (3 dB)	2° × 2°
Scanning speed	6 rotations min^{-1}
Off–nadir beam (microwave part and processing)	
Frequency	13.565 GHz
Pulse duration	50 μs
Frequency bandwidth	200 MHz
Pulse repetition frequency	4 kHz
Peak power	100 W
Range resolution after compression	0.75 m
Time integration/Number of integrated samples	37 ms/147

effect, we need to maximize the radar's inherent resolution (which is inversely proportional to the transmission bandwidth B_d) and/or maximize the number of independent samples, N_{int}, which is a product of the integration time T_{int} and the pulse repetition frequency. But B_d and T_{int} are also the result of trade-off, and B_d is reached by trading off $I(R)/B_T$ and pulse duration. Integration time T_{int} is limited by the curvature of the electromagnetic wavefront and the displacement due to the satellite's motion and antenna rotation of the horizontal sampled bins. The maximum value of T_{int} is mainly constrained by the required effective horizontal resolution ΔX (Jackson 1987):

$$T_{\text{int}} \leq \frac{\Delta X \sin\theta}{V(\beta_\phi/2)}, \tag{15a}$$

$$T_{\text{int}} \leq \frac{\Delta X tg\theta}{V(\beta_\theta/2)}, \tag{15b}$$

where V is the satellite velocity and β_θ is the 3-dB aperture in elevation.

Dimensioning must also factor in uncertainties regarding geophysical variables. To be able to generate a product to meet the needs of wave spectrum analysis (for modeling in particular), our objective is to limit resolution and uncertainties to values of the same order of magnitude as those obtained by buoys or used in models, that is, resolution better than 20% for wavelengths, resolution better than 15° for wave propagation direction, and uncertainty lower than 20% on spectral density (in each look direction).

Wavelength and directional resolution depend on the observation geometry (Jackson et al. 1985; Jackson and Walton 1985) whereas uncertainty on the spectral density is more closely related to the number of degrees of freedom used to estimate the directional wave spectrum and therefore to the number of individual estimates averaged to obtain the end product.

TABLE 2. Geometric characteristics and intrinsic performance of the system.

Footprint	18 km × 18 km
Scanning radius	88 km
Horizontal resolution	3.9–4.8 m
Signal-to-noise ratio of the time-integrated signal	8 dB (at center of lobe)
Displacement of resolution cell during integration time	0.9° in azimuth
Wavelength resolution for a wavelength of 200 m	30 m
Directional resolution	2°–3°

3) TECHNOLOGICAL CONSTRAINTS

The power budget requires a relatively high transmission peak power. Our research has attempted to reduce this constraint while maintaining an acceptable signal-to-noise ratio. A sensitivity study based on numerical simulations (see section 4) has shown that the optimum peak power level is 100 W. With the present technology, this is not compatible with the use of solid state power amplifiers (SSPA); only the traveling wave tube amplifiers (TWTA) technology is capable to provide such a power. Taking into account an overall efficiency of 20% for this type of amplifier and the mean power of the transmitter, the total power of the instrument remains below 250 W, which is the requirement for a minisatellite mission.

Table 1 shows the main features of the SWIMSAT system derived from the trade-off of the various parameters. These characteristics were obtained by using a set of analytical equations that describe the geometry, signal-to-noise ratio, speckle, and radar footprint displacement during the measurement integration time and by refining the results using a numerical simulation technique (see sections 3 and 4 for details of the simulation method and results). Note that the scanning is obtained by rotating only the feed horn of the antenna (about 300 g in rotation) while keeping the parabola fixed. The scanning speed chosen for SWIMSAT permits an overlap of the pattern described by the footprint on the surface in the along-track direction (see Fig. 1b), with distances between directions of observations separated by 180° in azimuth of the order of the radius of the pattern in the across-track direction. The geometric characteristics and intrinsic performances associated with this system are summarized in Table 2. In section 4, we discuss how we propose to reduce the uncertainties in the estimated wave spectra. The counterpart will be a reduction in the directional resolution up to 15°.

We calculated a mass and power budget, based upon the above characteristics, for the nadir and off–nadir spectrum beams. These results are shown in Table 3. The total power consumption and mass of the SWIMSAT instrument are consistent with the concept of a minisatellite with a power budget of approximately 250 W and a payload mass of about 50–100 kg.

TABLE 3. SWIMSAT mass and power budget.

	Power (W)	Mass (kg)
Microwave part (nadir)	22	10
Microwave part (off-nadir)	127	20
Processing (nadir)	42	12
Processing (off-nadir)	82	13
Antenna	4	19
Total	277	68

3. Simulation method

a. Overview

Our simulation aims to validate choices made on the basis of the analytical formula described above and to study the sensitivity of critical points in order to simulate the level of performance attainable with the chosen set of instrument and processing characteristics. This simulation focused on signal perturbations due to speckle and thermal noise.

The numerical study comprises a direct simulation step and an inversion step. Direct simulation includes a simulation of the sea surface and factors in the observation geometry, computation of the radar signal integrated over several samples, and speckle and thermal noise perturbations where applicable. Inversion simulation comprises calculation of the signal modulation and spectrum, corrected to allow for any perturbing effects (mean level of thermal noise and modulations due to speckle), and averaging of modulation spectra over an azimuth angle of 15°.

b. Sea surface simulation

By convention, we represent a surface perturbed by waves as a series of superimposed sine waves, each characterized by their amplitude, phase, and direction. For the purposes of our study, we will ignore phase relationships between surface components due, in particular, to hydrodynamic interactions. Indeed, at the wavelengths in our simulation (more than 10 m), such interactions can be considered negligible. Moreover, as we have seen in section 2a, hydrodynamic modulation can be ignored for a low-incidence radar beam. Consequently, we will assume that the sea surface is defined by a Gaussian probability density function in which the phases of each component are independent and equally distributed between 0 and 2π.

To simulate the backscattered signal in each radar range gate and look direction, we first calculate the slopes in the radar beam's look direction (*OX* axis). This direction varies as the beam rotates. We therefore run two surface simulations for slopes in the across-track (*Ox* axis) and along-track (*Oy* axis) directions. At each point on the surface and in each look direction, we then combine the *Ox* and *Oy* slopes to obtain the slopes $\xi_x(x, y)$ in the look direction *OX*:

$$\xi_x = \xi_x(x, y)\cos\phi + \xi_y(x, y)\sin\phi, \qquad (16)$$

where ξ_i is the local slope of the surface in the direction *i*, and ϕ is the angle (*Ox*, *OX*). The slope spectrum in the *x* direction is $k_x^2F(k_x, k_y)$, and the slope spectrum in the *y* direction is $k_y^2F(k_x, k_y)$.

The surface simulation comprises the following steps:

1) Generate a random sample of a variable to simulate Gaussian white noise, with mean 0 and variance 1.
2) Calculate the Fourier transform $B(k_x, k_y)$ of this noise, which has the property that its phases are uniformly distributed between 0 and 2π.
3) Multiply this normalized noise spectrum by the energy spectrum of the wave slopes to obtain a complex spectrum $S_p(k_x, k_y)$. For each component $k(k_x, k_y)$ of the slope spectrum $k_i^2F(k_x, k_y)$ ($i = x$ or y), the real part $\mathrm{Re}(S_p(k_x, k_y))$ and the imaginary part $\mathrm{Im}(S_p(k_x, k_y))$ of the complex slope spectrum $S_p(k_x, k_y)$ are given by

$$\mathrm{Re}(S_p(k_x, k_y)) = \sqrt{k_i^2F(k_x, k_y)}\frac{\mathrm{Re}[B(k_x, k_y)]}{\|B\|}$$

$$\mathrm{Im}(S_p(k_x, k_y)) = \sqrt{k_i^2F(k_x, k_y)}\frac{\mathrm{Im}[B(k_x, k_y)]}{\|B\|}, \qquad (17)$$

   where $\|B\|^2 = \mathrm{Re}(B(k_x, k_y))^2 + \mathrm{Im}(B(k_x, k_y))^2$ is the norm of the noise. The spectrum thus constructed has an amplitude $[k_i^2F(k_x, k_y)]^{1/2}$ and a phase ψ, which is uniformly distributed between 0 and 2π. The slope spectrum is defined as an even function between $-k_{\max}$ and $+k_{\max}$ to allow for the ambiguity of 180° in the direction of propagation.
4) Calculate the inverse Fourier transform of $S_p(k_x, k_y)$ to provide a realization of the surface slope for a given set of random phases.

The simulated surfaces cover 36 km × 36 km, which allows for the displacement of the radar footprint as measurements are acquired. The trade-off between the ground resolution and the number of sampling points resulted in a discretization of this surface by 2048 × 2048 points (i.e., horizontal sampling $\Delta X = 17.5$ m). This corresponds in the wavenumber domain to a maximum wavenumber $k_{\max} = 0.18$ rad m^{-1} and wavenumber resolution $dk = 2\pi/L_x = 1.745 \times 10^{-4}$ rad m^{-1}. The ideal horizontal resolution to simulate the surface would have been lower than the radar's horizontal resolution, which is about 3 m. But to simulate a radar footprint of 36 km × 36 km requires a large number of points (12 000 × 12 000), which involves a considerable amount of memory and CPU overhead. We therefore chose a resolution of about 18 m, which is about 6 times the radar's horizontal resolution. This characteristic is factored into the simulated radar signal (see section 3c).

The sea-state spectra used in our simulation correspond to two different cases, namely, fully developed sea and swell conditions. Table 4 gives the analytical form and conditions chosen in each case.

Figures 3 and 4 illustrate in the wind–sea and swell cases, respectively, a subsurface of 2 km × 2 km of the

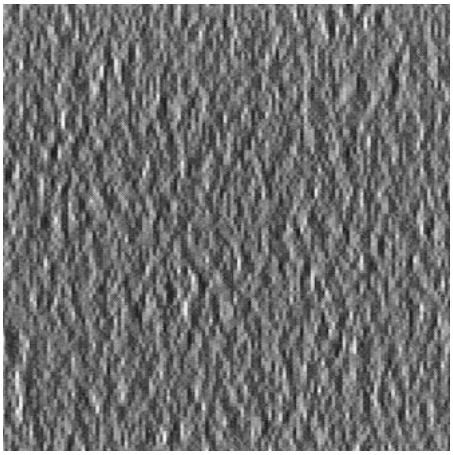

FIG. 3. Simulated sea surface for wind–sea case defined in Table 4. The direction of wave propagation is parallel to the horizontal axis. A subsurface of 2 km × 2 km of the total surface is represented here with a pixel size of 17.5 m × 17.5 m.

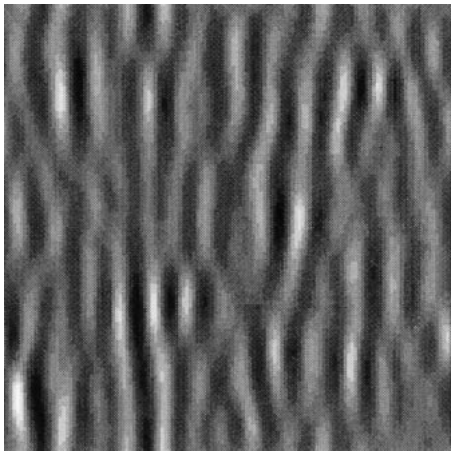

FIG. 4. Same as Fig. 3 but for the swell case defined in Table 4 (with $H_s = 4$ m).

simulated surface, with the direction of wave propagation parallel to the horizontal axis ($\phi_0 = 0$). Note that the swell simulation (Fig. 4) exhibits a pattern that is more regular than the wind–sea simulation (Fig. 3), with long crest lengths. This is because the swell spectrum is much narrower, both in terms of wave number and azimuth. In both cases, we checked that the correlation length of our simulated surface in the direction perpendicular to the wave propagation direction is well below the azimuth dimension of the radar footprint (18 km). This validates condition 3) of the modulation-spectrum to slope-spectrum transfer function (see section 2a). Indeed, this correlation length is about 80 m for the wind–sea case and 800 m for the swell case.

c. Radar signal simulation

1) BASIC PRINCIPLE

Simulating the radar signal means calculating, for a given look direction, the modulation $m(X)$ in the horizontal plane using Eq. (5) and the modulation $m(R)$ projected onto the radial plane. Speckle and/or thermal noise can be factored into the calculation. The signal $I(R)$ is derived from $m(R)$ using Eq. (13). This calculation is repeated for all samples (temporal integration). In this approach, the mean radar cross section $\tilde{\sigma}_0$ that would be observed in the absence of long waves was set at 6 dB, which is more or less the mean value obtained by the radar flown on the TRMM mission (K_u-band) at incidence angles near 10° (Meneghini et al. 1998). For our simulation, we chose to calculate the coefficient α using Eq. (4), where the slope probability density function is assumed to be Gaussian, and the associated variance υ is assumed to follow the results of Jackson et al. (1985):

$$\upsilon = 0.0028U + 0.009. \quad (18)$$

In short, the direct simulation consists of a) calculating the modulation $m(X)$ in a given look direction, b) calculating $m(R)$ by projecting $m(X)$ onto the radial plane (assuming a spherical earth), c) simulating speckle noise for a set of values of $m(R)$, d) calculating $I(R)$ from the set of simulations performed in step c), e) simulating the thermal noise applied to a set of values of $I(R)$, f) shifting samples to simulate the displacement of the horizontal cell over the integration time, and g) integrating several independent samples (temporal integration) with/without compensation of the range to account for the distance traveled by the satellite over the integration time. Depending on the simulation we ran, steps c), e), f), and g) were or were not performed.

2) SPECKLE SIMULATION

Speckle is a well-known phenomenon affecting radar data [see, e.g., Ulaby et al. (1982)]. To reduce fluctuations due to speckle, the received signal needs to be averaged over a certain number of echoes (N_{int}). In addition to temporal integration, SWIMSAT proposes to use a ''multilook'' technique that involves averaging the signal over several adjacent radial range gates. Since the radar's inherent horizontal resolution is about 4 m, and the required resolution for SWIMSAT is of the order of 20 m, we propose to average the received signal over 6 adjacent gates. To simulate the radar signal perturbed by speckle noise, we performed a random selection from samples of a Gamma function of six looks with a mean of $[1 + m(R)]$. Equation (13) then gives the intensity $I(R)$, assuming that $g(B_T)$ is zero. The results described below were obtained with an horizontal resolution Δx of 4 m (radar radial resolution = 0.75 m), an average over 6 adjacent gates, and a time integration over N_{int} 147 samples. The corresponding value of T_{int} ($T_{\text{int}} = 37$ ms) is the upper bound imposed by the displacement of the radar resolution cell during T_{int} if we are to maintain an actual resolution of about 26 m (Eqs. 15a,b).

3) THERMAL NOISE SIMULATION

The mean and variance of the thermal noise B_T are related to the system's equivalent temperature. The mean of B_T is given by Eq. (14). We simulate thermal noise, using the same method as for speckle, by performing a random selection from a Gamma function with six looks and calculating the signal $I(R)$ for each sample from Eq. (13), then integrating N_{int} samples.

4) SIMULATION OF FOOTPRINT DISPLACEMENT DURING MEASUREMENT

During the time of integration, there is a displacement of the footprint because of the satellite advection (rotation of the beam is not considered here). When the radar is looking perpendicular to the satellite track, the effect of the displacement is to broaden the azimuth footprint. Because of the large azimuth footprint (18 km), this effect remains negligible (about 1.5%). If the look direction is aligned along the satellite track, the horizontal surface elements corresponding to the range sampling are moved during time integration. For the conditions of SWIMSAT ($T_{\text{int}} = 37$ ms, velocity = 7 km s^{-1}), the horizontal distance between the first gate of the first and last echo in the along-track look direction is of the order of 260 m. If the received signal is integrated in the order in which gates are received, the sum of echoes is calculated from different surface positions. Such an integration procedure would filter out the wave signal. To avoid this effect, the real-time processing must integrate signals reflected from the same cell on the sea surface. To estimate the importance of this effect, we simulated the signal $I(R)$ of each radar pulse, allowing for the displacement of the radar footprint. For the temporal integration of $I(R)$, we considered two cases: with and without range compensation during the temporal integration.

d. Signal inversion and calculation of modulation spectrum

Working from the simulated signal power $I(R)$ received by the radar receiver, signal inversion for each look direction ϕ consists of h) correcting the mean thermal noise in the integrated signal $I(R)$, i) extracting the mean trend and signal modulation in each radial gate and each horizontal gate (by projection, assuming a spherical earth), j) calculating the modulation spectrum, k) correcting the modulation spectrum for speckle effects, l) calculating the angular means and converting them into a wave-height spectrum. To test the system's sensitivity to error sources, we left out steps h) and k) from the inversion in certain simulations. In step j), the Fourier transform is calculated in the given look direction for the full length in elevation of the 3-dB radar footprint, that is, 18 km (1024 points). In all the results presented below, we compare the modulation spectrum

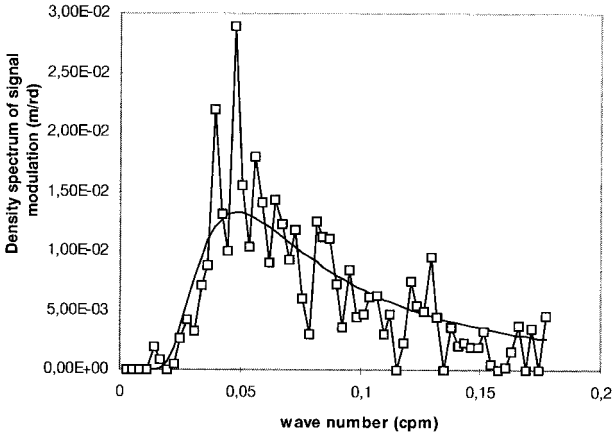

FIG. 5. Modulation spectrum retrieved for a non-noisy sample for the wind–sea case (square symbol) compared with the analytical modulation spectrum (no symbol).

retrieved after inversion with the modulation spectrum $P_m^s(k)$, obtained by omitting steps c), e), f), g), h), and k) (no noise or effects due to satellite motion), and with the ''reference'' modulation spectrum P_m^{ref}, defined by

$$P_m^{\text{ref}}(k, \phi) = \frac{\sqrt{2\pi}}{L_y}\alpha^2 k^2 F(k)G(\phi), \tag{19}$$

where $F(k)G(\phi)$ is the wave-height spectrum defined as the input for the sea surface simulation.

4. Results

In this section (up to section 4d), we present results for the fully developed wind–sea case (see Table 4) for a look direction aligned with the wave propagation direction. Results for different cases of sea state (including swell) are presented in section 4e, whereas the effect of combining several look directions is presented in section 4f.

a. Results ignoring noise and satellite motion effects

In our initial simulation, we studied the characteristics of the inverted modulation spectrum ignoring noise and other perturbing sources. We simulated the signal and computed the modulation spectrum without adding noise for a single pulse [steps a), b), d), i), and j) described above]. Figure 5 shows the modulation spectrum of the signal, $P_m^s(k)$, and the reference spectrum $P_m^{\text{ref}}(k)$. To reduce fluctuations in the simulated signal, we averaged the spectral density over eight resolution intervals $dk = 3.52 \times 10^{-4}$ rad m^{-1}. Our analysis, therefore, concerns spectra defined by 128 points and a resolution of 2.81×10^{-3} rad m^{-1}. The simulated modulation spectrum is in close agreement with the analytical reference spectrum (correlation coefficient = 0.90). The shape, spreading and peak of the theoretical spectrum are correct. However, the simulated modulation spectrum exhibits fluctuations with respect to the analytical spectrum, especially around the peak energy

TABLE 4. Sea-state spectra and wind–wave conditions used in the surface simulation.

	Nondirectional spectrum	Angular distribution	Wind–wave conditions
Fully developed wind sea	Pierson and Moskowitz (1964) $F(k) = \frac{0.008}{2} k^{-4} \exp\left[-\frac{5}{4}\left(\frac{k_{\text{peak}}}{k}\right)^2\right]$ $k_{\text{peak}} = 0.7\ g/U^2$	Jackson (1987) $G(\phi) = \frac{4}{3\pi} \cos^4(\phi - \phi_0)$	$U = 13$ m s^{-1} Corresponding H_s: 3.6 m, Corresponding k_{peak}: $2\pi/155$ m
Swell	Durden and Vesecky (1985) $F(k) = \frac{H_s^2}{16\sqrt{2\pi}\sigma_l} \exp\left[-\frac{1}{2}\left(\frac{k - k_{\text{peak}}}{\sigma_l}\right)^2\right]$	$G(\phi) = \frac{\cos^{14}(\phi - \phi_0)}{\int \cos^{14}(\phi - \phi_0)\, d\phi}$	$k_{\text{peak}} = 2\pi/200$ m $\sigma_l = 0.006$ rad m^{-1} $H_s = 4$ m or $H_s = 1$ m

level. This dispersion is probably due to the signal modulation being calculated for a radar footprint restricted to 3 dB and to numerical uncertainties in the simulation (particularly those generated by geometric projections and sampling necessary to translate from the radial to the horizontal plane).

b. Speckle effects

In accordance with Jackson et al. (1985) and Jackson and Walton (1985) and as detailed in the appendix, we can show that the spectrum of the received signal for each pulse is related to the signal's modulation spectrum by the following equation:

$$P_i(k) = \delta(k) + R(k)P_m(k) + P_s(k) + h(k), \qquad (20)$$

where $\delta(k)$ is the continuous component of the signal; $R(k)$ is the radar's impulse response; $P_m(k)$ is the signal modulation spectrum, as expressed by Eq. (6); $P_s(k)$ is the speckle spectrum; and $h(k)$ is a second-order term due to the speckle effect on the signal modulation. Assuming that the transmitted waveform is Gaussian, one obtains the following expressions for $R(k)$ and $P_s(k)$:

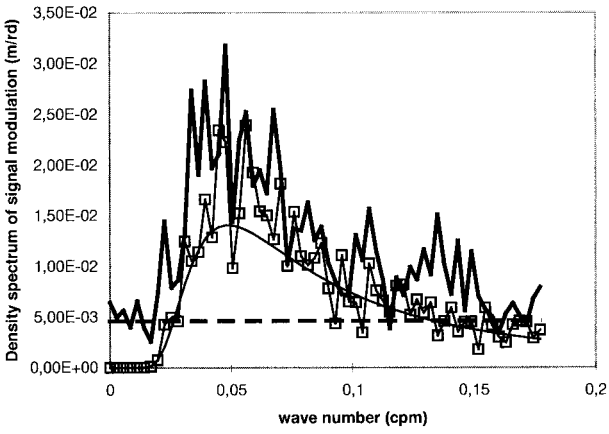

FIG. 6. Effect of speckle on simulated modulation spectrum. Bold line: simulation includes speckle but without correction of this effect in the inversion; squares: simulation does not include speckle; thin line: analytical modulation spectrum; (dotted line): speckle spectrum level according to Eq. (25).

$$R(k) = \exp\left(-\frac{k^2}{2k_p^2}\right), \qquad (21)$$

where $k_p = 2\sqrt{2\ln 2}/\Delta x$ and Δx is the system's inherent horizontal resolution, and

$$P_s(k) = \frac{1}{\sqrt{2\pi}k_p} \exp\left(-\frac{k^2}{2k_p^2}\right). \qquad (22)$$

Concerning $h(k)$, we obtain (see appendix)

$$h(k) = \frac{\sqrt{2}}{\sqrt{\pi}k_p}\left[\int R(k')R(k' - k)^2 P_m(k' - k)\, dk'\right]P_s(k). \qquad (23)$$

For SWIMSAT, $R(k)$ varies between 0.97 and 0.99 for wavelengths from 20 m to 1 km. Hereafter, we adopt an impulse response of unity. We also assume that the continuous part of the signal is prefiltered. Consequently, for a given pulse and look direction ϕ, the modulation spectrum of the signal affected by speckle noise is written as

$$P(k) \approx P_m(k) + P_s(k) + h(k). \qquad (24)$$

For a signal estimated from N_{int} independent samples, the speckle spectral density $P_s(k)$ is given by

$$P_s(k) = \frac{1}{N_{\text{int}}\sqrt{2\pi}} \frac{\Delta x}{2\sqrt{2\ln 2}}. \qquad (25)$$

Figure 6 presents results obtained under the same conditions as in Fig. 5 but simulating speckle for a signal integrated over 147 successive echoes and six radial range gates. The simulated modulation spectral density (thick lines) is systematically overestimated with respect to the reference level (thin line). This shows that we need to correct the speckle modulation spectrum. On the basis of these results, we calculated that the difference between the simulated spectrum ignoring speckle (square symbols) and the simulated spectrum allowing for speckle (thick line) is very close to the level of the speckle spectrum computed analytically from Eq. (25) (dashed line). We thus verify that to apply a speckle correction, we simply need to apply Eqs. (24)–(25), ignoring $h(k)$. We were able to calculate

$h(k)$ explicitly and independently in the simulation from Eq. (23). We found that $h(k)$ was negligible ($\approx 3.6 \times 10^{-4}$ in the case described here). This confirms the hypothesis put forward by Jackson and Walton (1985), which ignores $h(k)$ without estimating it. Even if we can correct the bias on the spectral density due to speckle, the presence of speckle noise restricts wave detection to wavelengths at which the modulation spectral density is greater than the speckle spectral density. Figure 6 shows that for the fully developed sea state with a 13 m s^{-1} wind speed, the detection threshold is $k_{\text{lim}} = 0.13$ rad m^{-1}, meaning that the smallest resolvable wavelength is approximately 50 m.

c. Thermal noise effect

The results presented here (Figs. 7a–c and 8a–c) were obtained by taking into account thermal noise and speckle noise (with $N_{\text{int}} = 147$, $\Delta x = 4$ m) in the generated radar signal. In the inversion step, a speckle correction is applied [Eqs. (24)–(25), ignoring $h(k)$], whereas a correction for the mean thermal noise level is applied in Figs. 8a–c but not in Figs. 7a–c. In the former case, the modulation spectrum is retrieved by applying a correction to allow for the mean thermal noise level, which is assumed known (but this correction does not account for thermal noise fluctuations). We considered three transmission power levels, 10, 30, and 100 W, shown in Figs. 7a–8a, 7b–8b, and 7c–8c, respectively. These levels correspond respectively to a signal-to-noise ratio $[I(R)/B_T]$ at the center of the radar footprint of -1.9 dB, 2.8 dB, and 8 dB. Our results show that if we do not apply any correction for the mean thermal noise, the simulated modulation spectral density is significantly underestimated with respect to the reference level (Figs. 7a–c) for all $I(R)/B_T$ values considered here. When the thermal noise correction is applied (Figs. 8a–c), the simulated modulation spectra are in closer agreement with the reference values. However, only the highest values of the simulated transmitted power gives acceptable errors: the relative error on the wave height variance in the look direction is 6%, 28%, and 190%, respectively, for transmission powers of 100, 30, and 10 W, that is, for signal-to-thermal noise ratios of 8 dB, 2.8 dB, and -1.9 dB, respectively.

These simulations show that it is necessary to apply a thermal noise correction to the radar signal for all $I(R)/B_T$ values considered. Moreover, the transmission power must be greater than 30 W at least [$I(R)/B_T >$ 2.8 dB] to retrieve the wave height spectrum with an acceptable degree of error. A transmission power of 100 W [$I(R)/B_T = 8$ dB] would render thermal noise errors negligible. Simulations also showed that the correction to allow for the mean thermal noise level B_T must be accurate to 5% or better. Current techniques for determining thermal noise enable us to estimate B_T to within 2%, so this result is not a constraining factor.

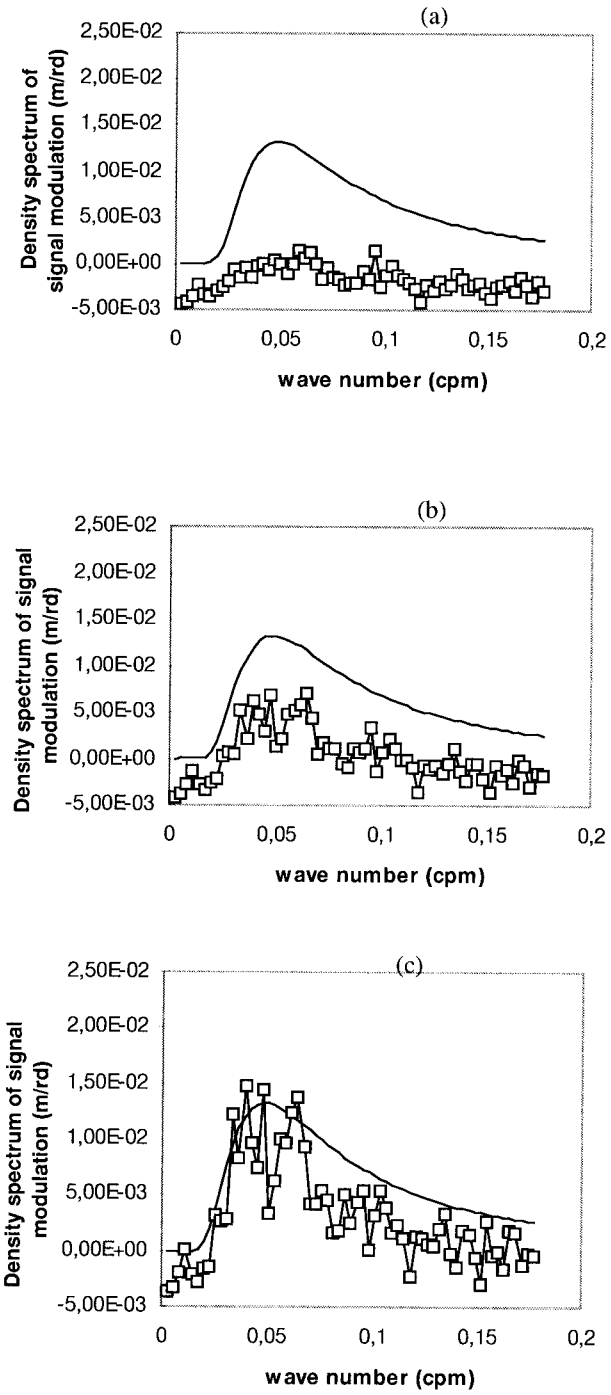

FIG. 7. Modulation spectra after inversion (lines with square symbols), in simulations factoring in speckle noise and thermal noise, for three transmission powers: (a) 10 W (b) 30 W, and (c) 100 W. Sea surface conditions are identical to those in Fig. 6. Solid line without symbol is for the analytical modulation spectra.

d. Effect of footprint displacement during measurement

As explained in section 3c, we considered several simulations. Figure 9 shows the effect of applying a

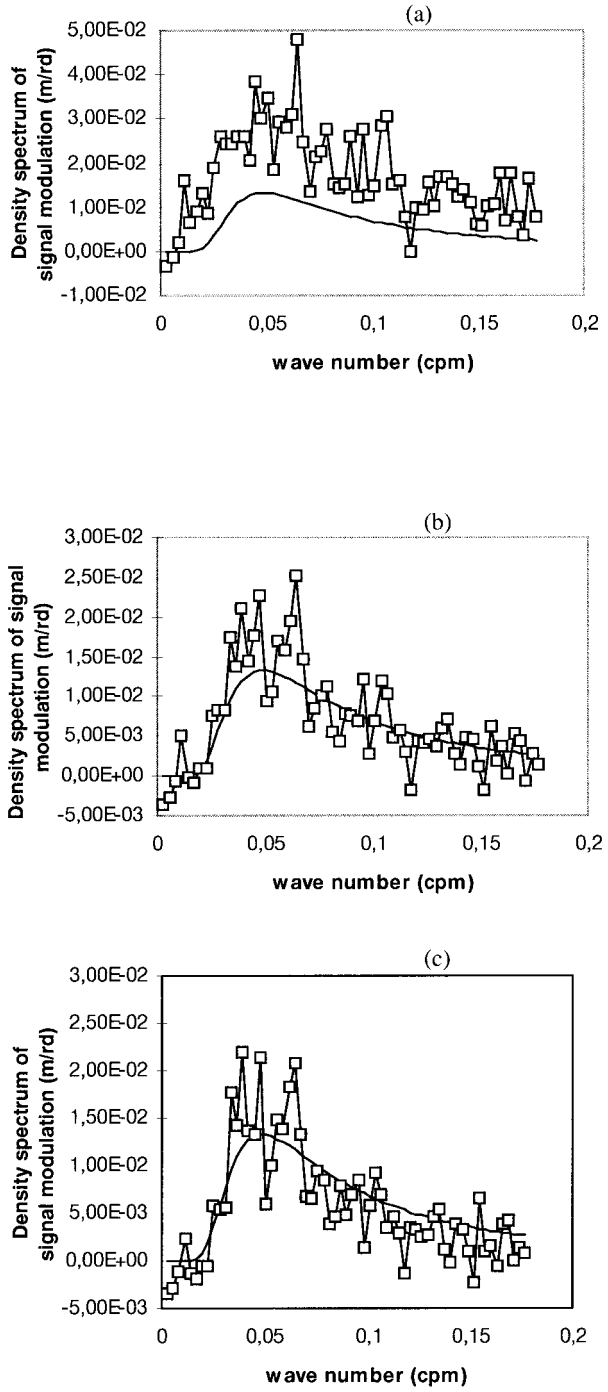

FIG. 8. Same as Fig. 7 but with added correction for mean thermal noise level in the retrieval procedure.

range correction to the temporal integration of radar echoes. In the first case (squares in Fig. 9), we applied no range compensation; in the second case (thin line in Fig. 9), we applied a range correction to the temporal integration. This correction consists of shifting the range gates of successive integrated echoes in order to integrate signals backscattered from the same surface element. In this calculation, we assumed a constant radar footprint displacement for all gates, as estimated from the gate at the center of the antenna lobe. These results clearly indicate the need to correct for the gate displacement over the sea surface when integrating the radar signal. We also tested other range correction algorithms. In particular, we applied a range shift calculated exactly for each gate (given the incidence angle and assuming a spherical earth). The results (not illustrated) do not differ significantly from those presented here. Thus, we find that a correction approximating the range migration over the integration time is sufficient. This correction is, nevertheless, essential to avoid filtering out the parameters we wish to retrieve.

e. Results including all perturbing effects

We now describe the simulation results we obtained with full inversion. The following effects were accounted for 1) temporal (147 samples) and spatial (6 range gates) integration of echoes with displacement of the radar footprint during the integration time, 2) simulation of speckle and thermal noise by random functions, and 3) inversion with correction to allow for radar footprint displacement, speckle noise correction, and mean thermal noise correction. The simulation configuration corresponds to the parameters given in Table 1 using $\sigma_0 = 6$ dB, a satellite altitude of 500 km, satellite speed of 7 km s^{-1}, and earth geometry approximated as a sphere. We ran four simulations with different sea state conditions. Case A is the wind–sea case as described in Table 4 and up to section 4d; case B is a swell case as described in Table 4, with $H_s = 4$ m and $U = 13$ m s^{-1}, case C is identical to case B, except that $H_s = 1$ m; and case D is identical to case C, except that $U = 5$ m s^{-1}. Note that although the swell spectrum is not wind dependent, wind effects are factored into the α coefficient [Eqs. (4, 18)] of the transfer function.

Figures 10a–d show that the level and shape of the simulated spectra are consistent with those of the reference spectra. Fluctuations about the reference values are nonetheless significant, yielding correlation coefficients between simulated and reference spectra of 0.82, 0.94, 0.76, and 0.76, respectively, for cases A, B, C, and D. The two cases exhibiting the most well-developed sea states (cases A and B) yield lower statistical fluctuations.

f. Reducing statistical fluctuations

As the above results show, simulated modulation spectra (and therefore simulated wave spectra) exhibit a significant fluctuation in spectral density about the analytical reference spectrum, particularly under wind–sea conditions. To reduce these fluctuations, we propose to average the modulation spectrum over an angular domain of 15°, corresponding to a total of 16 samples. Our results, presented in Figs. 11a–d, are compared to

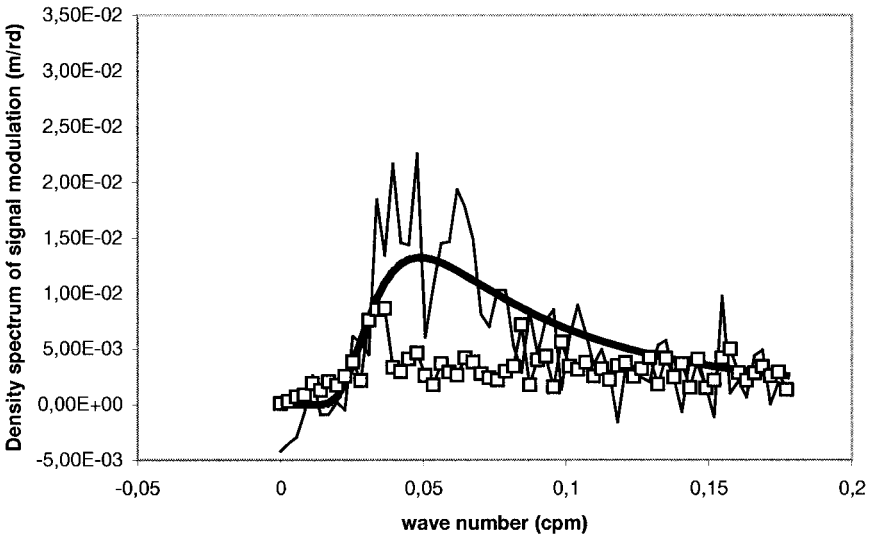

FIG. 9. Effect of applying correction for range displacement in the simulation. Line with square symbols: no correction for range migration during integration time. Thin line: includes correction for range migration (assumed constant throughout the spot beam). Bold line: analytical reference spectrum. Horizontal line: speckle level derived from Eq. (25).

the analytical reference spectrum, also averaged over 15°. The conditions are identical to those in Figs. 10a–d. By averaging over 16 samples, we succeeded in reducing the statistical fluctuations. The correlation coefficients between simulated and reference spectra are 0.92, 0.99, 0.95, and 0.96 for cases A, B, C, and D, respectively, that is, larger than without averaging (see section 4e). This increase in the correlation coefficient (and therefore the reduction in statistical fluctuation) is even clearer under calm sea conditions (cases C and D). Correlatively, the relative error on the wave height variance (calculated in the look direction) is 8%, 9%, 20%, and 20% for cases A, B, C, D, respectively. This corresponds to errors of less than 10% for the significant wave height, with the smallest relative errors in cases of large significant wave height (cases A and B). The speckle level (horizontal line in Figs. 11a–d) compared with that in the simulated spectra shows that in all cases but one (case C), most of the modulation spectrum is above the speckle level. The minimum detectable wavelength given by the minimum wavelength where the energy density is above the speckle level is about 50–70 m for the wind–sea case. For swell, all the energy density can be detected in case B (H_s = 4 m). Cases C and D, both with a significant wave height of 1 m but with different wind speeds, yield different results due to wind dependence and to the transfer function defining the relationship between the modulation spectrum and wave-height spectrum [Eqs. (4, 18)]. The high wind speed case (case C) is the least amenable to simulating swells with a significant wave height of the order of 1 m.

So, our results show that SWIMSAT should be capable of measuring wave spectral properties under wind–sea, provided the dominant wavelength is greater than about 70 m, and in swell conditions, provided the significant wave height is greater than 1.5–2 m, depending on wind. We have shown that provided that an averaging process is applied, the inversion process would give an accuracy of about 20% in wave energy (10% in wave height). Resolution in direction is 15° after the averaging process is applied, whereas resolution in wavelength is about 20% of the wavelength, as explained in section 3. Due to the sampling variability, determination of the peak of the spectrum is also subject to some uncertainty. Results presented here (Fig. 11) indicate that some smoothing process will be necessary to automatically extract the peak wavelength but that the accuracy in the estimate of the peak should be of the order of the wavelength resolution.

5. Conclusions

In this paper we have described the measurement principle and main features of the SWIMSAT radar designed to provide satellite-based measurements of wave spectral properties. This principle is based not on a synthetic aperture radar (SAR) but on a real-aperture antenna with a low-incidence beam (10°) scanning through 360° azimuth. The transfer function defining the relationship between the modulation spectrum of the radar signal and the wave spectrum is therefore dependent on the tilt modulation alone. For our study, we developed a simulation method for studying the sensitivity of wave spectra retrieved for a given radar observation configuration (spatial resolution, signal-to-noise ratio, integration time, etc.) and inversion processing configuration (factoring in noise sources and range displacements during temporal integration). This

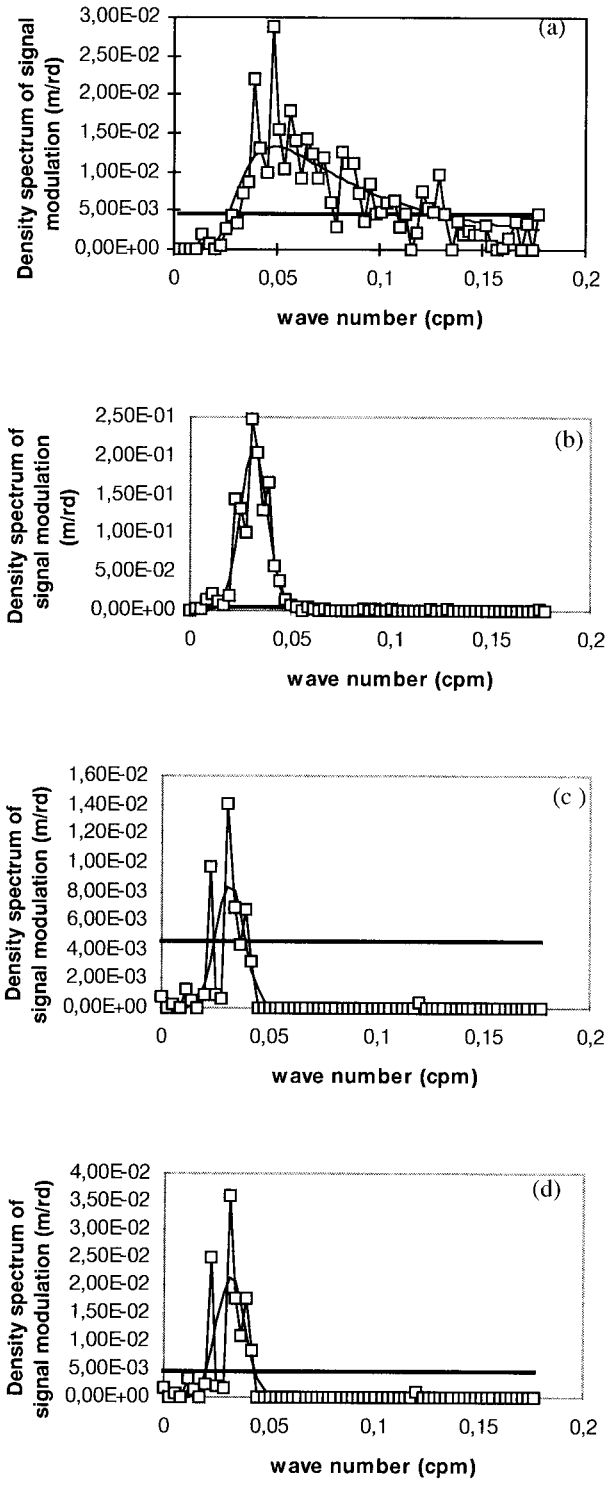

FIG. 10. Fully simulated modulation spectra for a given look direction ϕ (lines with square symbols). Thin line without symbols: analytical reference spectrum. (a), (b), (c), (d): sea-state conditions for cases A, B, C, and D, respectively.

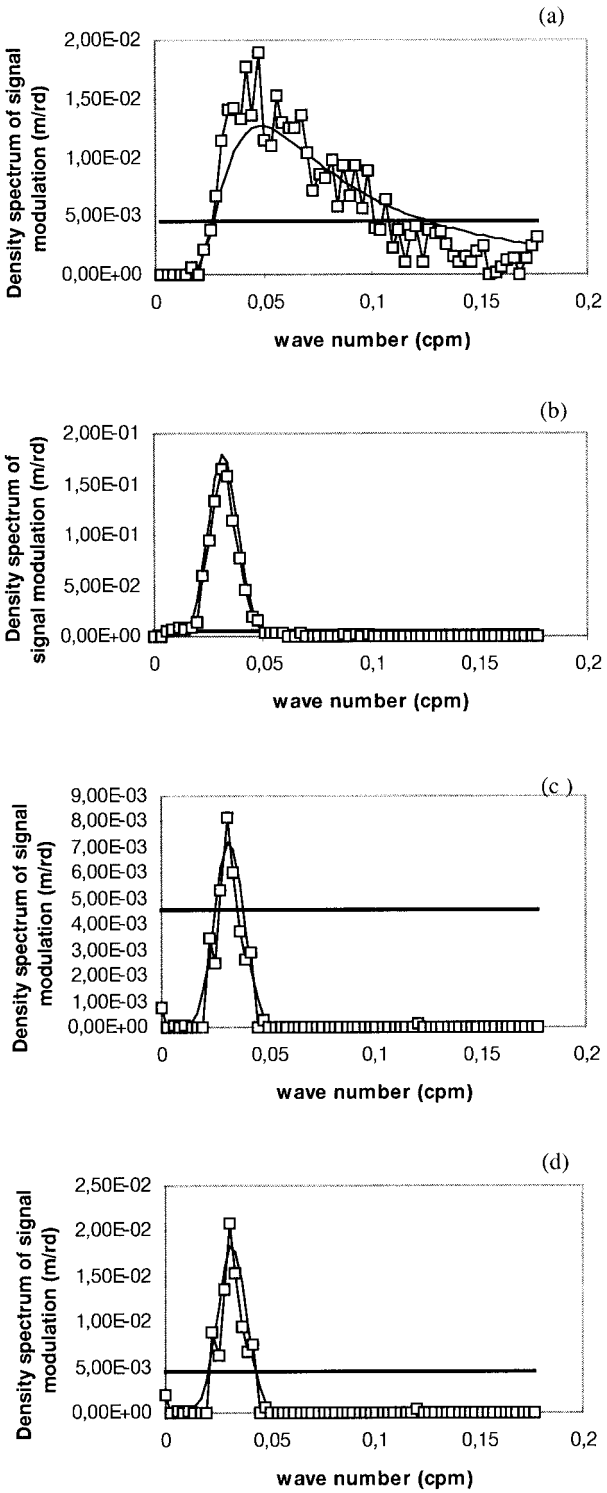

FIG. 11. Same as Fig. 10 but for results obtained from averaging over 16 samples, covering 15° azimuth.

study has validated the proposed radar concept and refined its characteristics.

Our study of speckle noise effects confirmed that a speckle spectrum correction must be applied in the processing and that this correction can be achieved simply with Eqs. (24)–(25) by ignoring the second-order term $h(k)$. To minimize speckle effects, we propose to integrate the signal over time (37 ms, i.e., 147 independent samples) and radial range (6 consecutive gates).

Our study of sensitivity to thermal noise highlighted the need to apply a thermal noise correction. Such a correction implies that we must develop a suitable method for estimating this noise for the SWIMSAT instrument. Simulations demonstrated that a signal-to-noise ratio of 8 dB at the center of the antenna lobe (transmitted power = 100 W) yields satisfactory results under varying sea-state conditions. Our simulations also showed the need to apply a correction to the radar signal during temporal integration of the satellite's motion, and we have suggested a simple method to achieve this.

Finally, we showed that it is possible to reduce uncertainties in simulated spectra by averaging over several samples corresponding to an angular sector of the radar beam scan. A good trade-off between uncertainty and final resolution of the geophysical data product seems to be achieved by averaging the signal spectrum over 15° azimuth (i.e., 16 samples).

The simulations show that SWIMSAT should be capable of measuring wave spectral properties under wind–sea (provided the dominant wavelength is greater than about 70 m) and swell conditions (provided the significant wave height is greater than 1.5–2 m, depending on wind). We did not simulate cases where the sea surface is not fully developed. We can extrapolate these results and say that SWIMSAT should be able to provide measurements in such cases only if the dominant wavelength is greater than 70–100 m. In all these cases, the direction of wave propagation with respect to the observation geometry has no effect. This is an advantage with respect to SAR observations, where data inversion in terms of wave spectra is still very limited, particularly for standard spaceborne SAR altitudes (700–800 km), and for waves with a component propagating in the along-track direction. It would thus seem that SWIMSAT could provide data to complement SAR data, as it would enable us to overcome the nonlinear effects of the SAR transfer function and the associated limit imposed by current spaceborne SAR observations to measure waves smaller than about 200 m in wavelengths.

SWIMSAT has been designed to be compatible with the concept of ''small-satellite'' missions (satellite typically of less than 500 kg). With the development of this type of mission in the future by the various space agencies, there are several opportunities to propose this instrument, which will provide very useful observations to complement other planned missions devoted to the ocean surface based either on SAR or on altimeter systems. As expressed by the marine community, there is obviously a gap to fill to improve observation and prediction of the spectral properties of waves.

Acknowledgments. This study was completed with the financial support of the French space agency CNES (Centre National d'Etudes Spatiales) and Alcatel Space Industries. We wish to thank Gérard Caudal for his helpful comments during the development of this study.

APPENDIX

Backscattered Power Spectrum

Following Jackson et al. (1985), we can write that for any transmitted pulse, the backscattered field, e, of a finite-duration transmitted pulse, e_0, as a function of surface range x is given by

$$e(x) = C \int e_0(x - x')g(x')\, dA(x'), \qquad \text{(A1)}$$

where C is a constant associated with the radar characteristics and the impulse response of the surface is proportional to $g(x)dA(x)$, $dA(x)$ is the reflectivity density of the surface in the absence of large-wave modulations; and $g(x)$ is the reflectivity modulation due to the tilt of the large waves.

Assuming that the reflectivity density of the surface can be modeled as a Gaussian noise process and taking into account the fact that the coherency distance is small compared to the surface range resolution Δx [$\Delta x = (c\Delta\tau/2)\sin\theta$], dA can be described by a delta-function autocovariance

$$\langle dA(x)dA^*(x)\rangle = \sigma_0\delta(x' - x)dxdx', \qquad \text{(A2)}$$

where $\delta(x)$ is the Dirac function, σ_0 the normalized radar cross section, and the asterisk denotes the complex conjugate.

For large beam extents (as is the case for SWIMSAT), the reflectivity modulation can be modeled as a first-order perturbation:

$$g(x)^2 = 1 + m(x). \qquad \text{(A3)}$$

If the detected power is w [$w(x) = |e(x)|^2$], then it follows from (A1) that the average backscattered power is given by

$$w_0 = \langle w(x)\rangle = C^2\sigma_0 \int |e_0(x)|^2\, dx. \qquad \text{(A4)}$$

The spectrum of the backscattered power is then given by the Fourier transform of the autocovariance of the normalized backscattered power:

$$P(k) = FT(R_{ww}(x)/w_0). \qquad \text{(A5)}$$

The explicit formulation of $P(k)$ is based upon the computation and simplification of the autocovariance function. We did these calculations using the definitions of

the fourth-moment of a Gaussian distribution and the properties of the convolution. We finally obtained

$$P(k) = \delta(k) + R(k)P_m(k) + P_s(k) + h(k), \quad \text{(A6)}$$

with

$$R(k) = \frac{\left|\int E_0(k')E_0(k' - k)\,dk'\right|^2}{\left|\int |E_0(k)|^2\,dk\right|^2}, \quad \text{(A7)}$$

$$P_s(k) = \frac{\int |E_0(k')|^2 \cdot |E_0(k' - k)|^2\,dk'}{\left|\int |E_0(k)|^2\,dk\right|^2}, \quad \text{(A8)}$$

$$h(k) = \frac{\int E_0(k') \cdot |E_0(k' - k)|^2 P_m(k' - k)\,dk'}{\left|\int |E_0(k)|^2\,dk\right|^2} \times E_0^*(k), \quad \text{(A9)}$$

where $E_0(k)$ is the Fourier transform of the pulse waveform $e_0(x)$, $R(k)$ the radar response function, $P_s(k)$ the power spectrum of speckle noise, and the asterisk denotes the complex conjugate. To simplify Eqs. (A7)–(A9), it is then assumed that the pulse waveform is Gaussian:

$$e_0(x) = \exp\left(-\frac{x^2}{2\Delta x'^2}\right). \quad \text{(A10)}$$

Then $E_0(k)$ is given by,

$$E_0(k) = \frac{1}{\sqrt{2\pi}k_p}\exp\left(-\frac{k^2}{2k_p^2}\right), \quad \text{(A11)}$$

with

$$k_p = \frac{2\sqrt{2\,\ln 2}}{\Delta x}. \quad \text{(A12)}$$

Combining (A1)–(A12) with (A7)–(A9) gives

$$R(k) = \exp\left(-\frac{k^2}{2k_p^2}\right), \quad \text{(A13)}$$

$$P_s(k) = \frac{1}{\sqrt{2\pi}\cdot k_p}\exp\left(-\frac{k^2}{2k_p^2}\right), \quad \text{(A14)}$$

$$h(k) = \frac{1}{\pi k_p^2}\exp\left(-\frac{k^2}{2k_p^2}\right)\int \exp\left(-\frac{k'^2}{2k_p^2}\right)\exp\left(-\frac{(k' - k)^2}{2k_p^2}\right)P_m(k' - k)\,dk'$$
$$= \left\{\frac{1}{k_p}\sqrt{\frac{2}{\pi}}\int \exp\left(-\frac{k'^2}{2k_p^2}\right)\exp\left(-\frac{(k' - k)^2}{2k_p^2}\right)P_m(k' - k)\,dk'\right\}P_s(k), \quad \text{(A15)}$$

where P_m is the density spectrum associated with the modulation of the surface waves. We did numerical calculations of $h(k)$ for each simulated case of P_m. Our results show that $h(k)$ remains negligible with respect to the other terms of Eq. (A6).

REFERENCES

Alpers, W. R., R. D. Ross, and C. L. Rufenach, 1981: On the detectability of ocean surface waves by real and synthetic aperture radar. *J. Geophys. Res.*, **86** (C7), 6481–6498.

Breivik, L.-A., and M. Reistad, 1994: Assimilation of ERS-1 altimeter wave heights in an operational numerical wave model. *Wea. Forecasting*, **9,** 440–451.

——, ——, H. Schyberg, J. Sunde, H. E. Krogstad, and H. Johnsen, 1998: Assimilation of ERS SAR wave spectra in an operational wave model. *J. Geophys. Res.*, **103** (C4), 7887–7900.

Brüning, C., S. Hasselmann, K. Hasselmann, S. Lehner, and T. Gerling, 1994: A first evaluation of ERS-1 synthetic aperture radar wave mode data. *Global Atmos. Ocean Syst.*, **2,** 61–98.

de la Heras, M. M., G. Burgers, and P. A. E. M. Janssen, 1994: Variational wave data assimilation in a third-generation wave model. *J. Atmos. Oceanic Technol.*, **11,** 1350–1369.

Durden, S. L., and J. F. Vesecky, 1985: A physical radar cross-section model for a wind-driven sea with swell. IEEE *J. Oceanic Eng.*, **OE-10,** 445–451.

Engen, G., and H. Johnsen, 1994: Directional wave spectra by inversion of ERS-1 synthetic aperture radar ocean imagery. *IEEE Trans. Geosci. Remote Sens.*, **32,** 340–352.

——, and ——, 1995: SAR-ocean wave inversion using image cross-spectra. *IEEE Trans. Geosci. Remote Sens.*, **33,** 1047–1056.

Eymard, L., and Coauthors, 1996: Study of the air–sea interactions at the mesoscale: The SEMAPHORE experiment. *Ann. Geophys.*, **14,** 986–1015.

Hasselmann, K., and S. Hasselmann, 1991: On the non-linear mapping of ocean wave spectrum into a SAR image spectrum and its inversion. *J. Geophys. Res.,* **96** (6) 10 713–10 729.

Hasselmann, S., C. Brüning, K. Hasselmann, and P. Heimbach, 1996: An improved algorithm for the retrieval of ocean wave spectra from synthetic aperture radar image spectra. *J. Geophys. Res.,* **101** (C7) 15 615–16 629.

Hauser, D., and G. Caudal, 1996: Combined analysis of the radar cross-section modulation due to the long ocean waves around 14° and 34° incidence: Implication for the hydrodynamic modulation. *J. Geophys. Res.,* **101** (C11), 25 833–25 846.

——, ——, G. J. Rijckenberg, D. Vidal-Madjar, G. Laurent, and P. Lancelin, 1992a: RESSAC: A new airborne FM/CW radar ocean wave spectrometer. *IEEE Trans. Geosci. Remote Sens.,* **30,** 981–995.

——, ——, and B. Chapron, 1992b: Observations with the RESSAC airborne radar during René 91. *Proc. ERS-1 Geophysical Validation Workshop,* ESA WPP-36, Penhorst, France, European Space Agency, 47–53.

——, ——, and L. K. Shay, 1995: Behavior of the ocean radar cross-section at low incidence, observed in the vicinity of the Gulf Stream. *IEEE Trans. Geosci. Remote Sens.,* **33,** 162–171.

Jackson, F. C., 1981: An analysis of short pulse and dual frequency radar techniques for measuring ocean wave spectra from satellites. *Radio Sci.,* **16,** 1385–1400.

——, 1987: The Radar Ocean–Wave Spectrometer. *Johns Hopkins APL Tech. Dig.,* **8,** 116–127.

——, and T. W. Walton, 1985: A comparison of *in situ* and airborne radar observations of ocean wave directionality. *J. Geophys. Res.,* **90** (C1), 1005–1018.

——, and D. R. Lyzenga, 1990: Microwave techniques for measuring directional wave spectra. *Surface Waves and Fluxes,* G. L. Geernaert and W. J. Plant, Eds., Vol. 2, Kluwer Academic, 221–264.

——, T. W. Walton, and P. L. Baker, 1985: Aircraft and satellite measurement of ocean wave directional spectra using scanning-beam microwave radars. *J. Geophys. Res.,* **90** (C1), 987–1004.

Janssen, P. A. E. M., P. Lionello, M. Reistad, and A. Hollingsworth, 1989: Hindcasts and data assimilation studies with the WAM model during the SEASAT period. *J. Geophys. Res.,* **94** (C1), 973–993.

Krogstadt, H. E., O. Samset, and P. W. Vachon, 1994: Generalizations of the non-linear ocean-SAR transformation and a simplified SAR inversion algorithm. *Atmos.–Ocean,* **32,** 61–82.

Lionello, P., and H. Günther, 1992: Assimilation of altimeter data in a global third-generation model. *J. Geophys. Res.,* **97** (C9), 14 453–14 474.

Mastenbroek, C., V. K. Makin, A. C. Voorrips, and G. J. Komen, 1994: Validation of ERS-1 altimeter wave height measurements and assimilation in a North Sea wave model. *Global Atmos. Ocean Syst.,* **2,** 163–184.

Meneghini, R., T. Iguchi, T. Kosu, L. Liao, K. Okamoto, and J. A. Jones, 1998: Use of the surface reference technique for path-attenuation estimate from the TRMM radar. *Proc. Symp. on the Precipitation Observation from Non-sun-synchronous Orbit,* Nagoya, Japan, Nagoya University, 163–168.

Pierson, W. J., and L. Moskowitz, 1964: A proposed spectral form for fully developed wind sea based on the similarity theory of S. A. Kitaigorodskii. *J. Geophys. Res.,* **69,** 5181–5190.

Soussi, E., 1997: Contribution à la spécification et analyse des performances du système VAGSAT pour la mesure spatiale des vagues à partir d'un radar à ouverture réelle. Doctoral thesis, Université Paris 6, 221 pp.

Ulaby, F. T., R. K. Moore, and A. K. Fung, 1982: *Microwave Remote Sensing.* Vol. II. Addison-Wesley, 1064 pp.

Valenzuela, G. R., 1978: Theories for the interaction of electromagnetic and oceanic waves—A review. *Bound.-Layer Meteor.,* **13,** 61–85.

Voorrips, A. C., V. K. Makin, and S. Hasselmann, 1997: Assimilation of wave spectra from pitch-and-roll buoys in a North Sea wave model. *J. Geophys. Res.,* **102** (C3), 5829–5849.